IEEE Photonics Journal
An IEEE Photonics Society Publication

Open Access

Gold Elliptic Nanocavity Array Biosensor With High Refractive Index Sensitivity Based on Two-Photon Nanolithography

Volume 7, Number 1, February 2015

Jun Yuan
Hong-Zhong Cao
Yi-Yang Xie
Zhao-Xin Geng
Qiang Kan
Xuan-Ming Duan
Hong-Da Chen

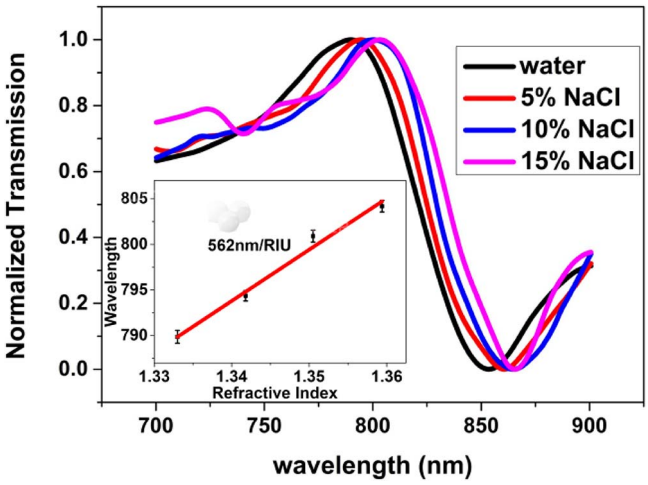

DOI: 10.1109/JPHOT.2014.2366167
1943-0655 © 2014 IEEE

IEEE photonics SOCIETY

IEEE

Gold Elliptic Nanocavity Array Biosensor With High Refractive Index Sensitivity Based on Two-Photon Nanolithography

Jun Yuan,[1] Hong-Zhong Cao,[2,3] Yi-Yang Xie,[1] Zhao-Xin Geng,[1,5] Qiang Kan,[4] Xuan-Ming Duan,[2,3] and Hong-Da Chen[1]

[1]State Key Laboratory of Integrated Optoelectronics, Institute of Semiconductor, Chinese Academy of Sciences, Beijing 100083, China
[2]Laboratory of Organic NanoPhotonics and Key Laboratory of Functional Crystals and Laser Technology, Technical Institute of Physics and Chemistry, Chinese Academy of Sciences, Beijing 100190, China
[3]Chongqing Institutes of Green and Intelligent Technology, Chinese Academy of Sciences, Chongqing 400714, China
[4]Key Laboratory of Semiconductor Materials, Institute of Semiconductor, Chinese Academy of Sciences, Beijing 100083, China
[5]School of Information Engineering, Minzu University of China, Beijing 100081, China

DOI: 10.1109/JPHOT.2014.2366167

Manuscript received September 1, 2014; revised October 21, 2014; accepted October 27, 2014. Date of publication October 31, 2014; date of current version December 30, 2014. This work was supported by the National Key Basic Research Program of China under Grant 2010CB934104; by the National Natural Science Foundation of China under Grant 61036009, Grant 61378058, Grant 61335010, and Grant 61036002; by the China Postdoctoral Science Foundation under Grant 2014M550796; and by the Science and Technology Research Funding of State Cultural Relics Bureau under Grant 20110135. Corresponding authors: Y.-Y. Xie and H.-D. Chen (e-mail: yiyangxie@semi.ac.cn; hdchen@semi.ac.cn).

Abstract: Metallic nanostructure arrays have been highlighted by their tremendously promising applications, such as biosensors, light harvesting, and fluorescence enhancement. To reach the aim of obtaining an inexpensive gold elliptic nanocavity array (GENA) biosensor, which has high refractive index sensitivity, the two-photon nanolithography, with the advantages of high resolution, low cost, time-saving, etc., is used to fabricate GENAs. The characteristics of these GENA biosensors are experimentally and theoretically investigated. A finite-difference time-domain method is applied to analyze the GENAs' localized surface plasmon resonance modes in the transmission spectra of GENAs and steady-state field intensity distributions. The refractive index sensitivities of the GENAs are characterized by the transmission spectra of GENAs in water and varied concentrations of NaCl solution. The results illustrate that the GENA biosensor under coupled mode sensing has high refractive index sensitivity, which reaches 562 nm/RIU.

Index Terms: Two-photon nanolithography, biosensor, gold elliptic nanocavity arrays, coupled mode.

1. Introduction

Plasmonic nanostructure arrays with metallic nanoholes and nanoslits can tremendously enhance the local electric field closes to the surface of the metallic nanostructure arrays. This phenomenon is due to the surface plasmon resonance (SPR) and the localized surface plasmon resonance (LSPR) that results from the collective oscillation of free conduction electrons in the metal. These electrons are excited by the specialized illumination light and, at the same time,

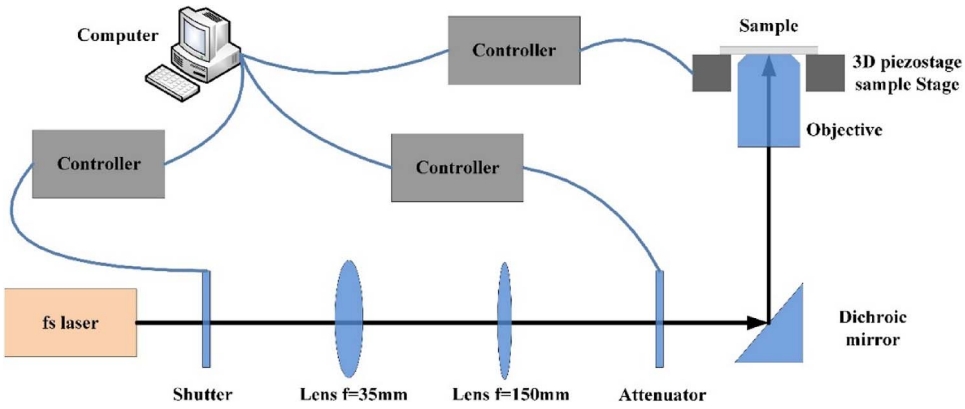

Fig. 1. The schematic diagram of the TPNL setup.

enhance the transmission of the light. This process is called extraordinary optical transmission (EOT) [1]–[3]. The optical and plasmonic properties of metallic nanostructure arrays strongly rely on the size, shape and the refractive index of surrounding medium [4]–[6]. This attractive optical property of the metallic nanostructure arrays has led to manifold applications such as sensing, light harvesting, optical switching and fluorescence enhancement [7]–[10]. Especially, the subwavelength confinement of the electric field offers a sensitive area for the refractive index of medium adjacent to the surface of nanostructures [11], [12].

Moreover, recent improvements in the metallic nanofabrication technology have led to a wide variety of design and fabrication of highly sensitive nanostructure biosensors [13], [14]. There are three common types of fabrication technologies: 1) self-assembly technology (e.g., colloidal nucleation and growth [15] and nanosphere lithography [16]) and 2) replication technology (e.g., nanoimprint [17]), 3) pattern direct writing technology (e.g. electron beam lithography (EBL) [18], focused ion beam (FIB) [19], and two-photon nanolithography (TPNL) [20]). The self-assembly technology is time-saving and inexpensive, but nanostructure defects are easily formed. Meanwhile, it is difficult to fabricate nanostructure with arbitrary designed patterns. The replication technology is time-saving and is capable of producing large-area well-organized nanostructures. However, the nanoimprint template of the nanostructure is expensive and easily broken. In contrast, the pattern direct writing technology easily reproduces the same nanostructures, but could not produce large-area orderly nanostructure. Whereas, it is time-consuming and expensive and complex equipment is required, such as EBL and FIB. The TPNL is an economical and powerful maskless method to fabricate nanostructures. In addition, TPNL could be applied for high resolution and intrinsic 3-D micro-structure fabrication [21], [22].

The focus of our research is to achieve a high refractive index sensitivity gold elliptic nanocavity arrays (GENAs) biosensor by using the low cost and less time consumption TPNL method. The sensing characteristics of the GENA are investigated theoretically and optimized through selecting the suitable LSPR modes. The GENAs are fabricated by TPNL technology and the polydimethylsiloxane (PDMS) microchannels are bonded onto the top surface of the GENAs. The refractive index sensitivity is measured by optical spectrum transmission measurement systems. Finally, the refractive index sensitivities of the GENAs are analyzed.

2. Experimental Details

The GENAs were fabricated by a TPNL technique. As shown in Fig. 1, the TPNL was carried out by a tightly focused femtosecond laser beam. A mode-locked Ti: sapphire laser system (Tsunami, Spectra-Physics) with a center wavelength of 780 nm, a pulse width of 80 fs, and a repetition rate of 80 MHz, was employed as a light source. The light from the laser system was expanded by two lens and entered into a high numerical aperture oil-immersed objective (Olympus, 100×, NA = 1.45). The incident light of the objective was tightly focused into the positive

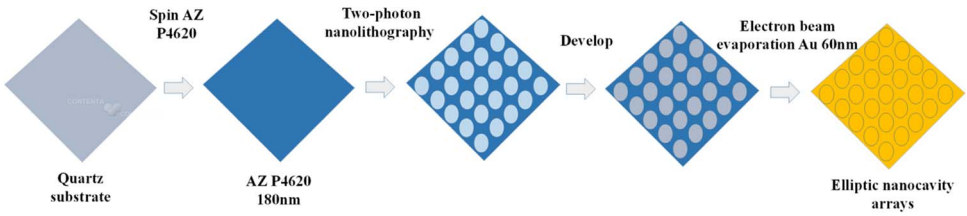

Fig. 2. A schematic view of the fabrication processes of GENAs.

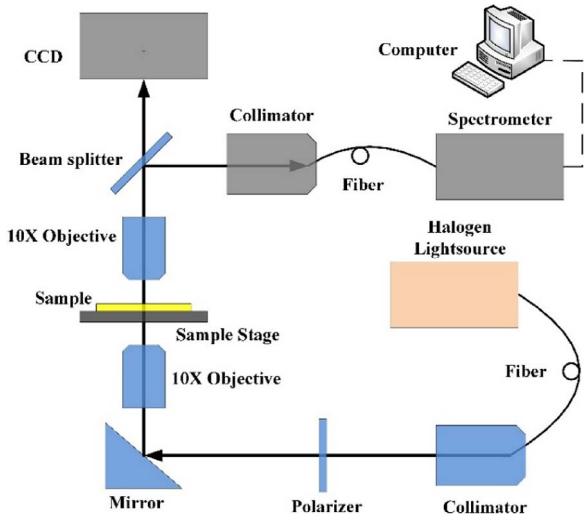

Fig. 3. The schematic diagram of the transmission spectrum measurement setup.

AZ P4620 photoresist film. A 3-D piezostage (Physik Instrumente P-563.3 CL) was employed to realize precise movement of the processed sample. An attenuator and a shutter were used to control the exposure time and exposure intensity, respectively.

The detailed fabrication processes are following. 1) A quartz glass was successively cleaned in acetone, ethanol, and the mixed solution of sulfuric acid and hydrogen peroxide which was set at a 3 : 1 ratio. 2) A 180 nm thick AZ P4620 photoresist was spin-coated on the substrate under the speed of 4000 rpm. 3) TPNL was used to pattern different sizes of elliptical nanohole arrays on the layer of AZ P4620 photoresist. 4) The photoresist was developed in the 1 : 4 diluted AZ 400K (AZ Electronic Materials) at room temperature, then the elliptic nanohole arrays of the photoresist were formed on the chip. 5) 3 nm Ti (adhesive layer) and 60 nm Au were successively deposited on the chip by electron beam evaporation (EBE). Fig. 2 is a detailed schematic diagram of the fabrication processes.

The optical transmission spectral measurements system is shown in Fig. 3. The test principle is briefly described as below. A light beam from a broadband tungsten halogen source (Ocean Optics HL-2000) was collimated by a collimator and successively goes through a Glan-Taylor polarizer, a silver reflecting mirror and focused on the pattern of GENA sample by a long-working-distance 10$\times$ objective. The sample stage allowed micron-resolved displacement, to adjust the position of the sample. The transmission light beam was collected and focused by another long-working-distance 10$\times$ objective and then split into two beams by a splitter, which were detected by a CCD camera and the spectrometer. The location of the light spot on the sample could be observed by the CCD camera. Meanwhile, the data of the transmission spectra were transferred from the spectrometer to the computer.

The refractive index sensitivity of the GENA biosensors was measured with water and the different concentrations of NaCl solution (5%, 10%, and 15%) covering the surface of the

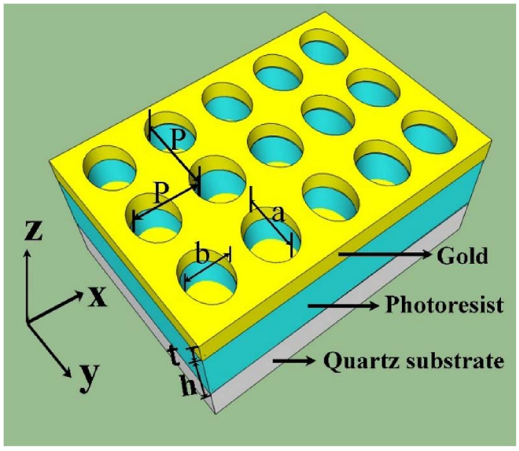

Fig. 4. Schematic of the GENAs arranged in a two-dimension square lattice.

biosensor chip. The refractive indexes of water and NaCl solution (5%, 10%, and 15%) are 1.3333, 1.3418, 1.3505, and 1.3594, respectively. To easily inject the sample to the surface of nanostructure sensing unit, a PDMS cover with microchannels was bonded onto the surface of the quartz glass with nanostructure sensing unit.

3. Results

According to our previous work, the TPNL technology is applied to fabricate various nanostructures, such as nanohole, nanodisk, nanoslit [23], [24]. Although all of the nanostructures can be used to fabricate refractive index sensors, the reflective index sensitivity of the nanorods are about 100 $\sim$ 300 nm/RIU which is smaller than the nanoholes reflective index sensitivity from 400 $\sim$ 700 nm/RIU [17], [25]–[27]. The high reflective index sensitivity of the nanoholes is because many modes can be excited and couple each other to generate the Fano resonances. As the same reason of the nanohole, The nanostructure coupled with nanohole and nanodisk coupled structure's reflective index sensitivity reaches more than 1000 nm/RIU [12], [28]. Therefore, the GENAs, arranged in a two-dimension square lattice, are adopted in this work. As illustrated in Fig. 4, the key structural parameters of the GENAs are labeled, including semi-major axis a (y-direction), semi-minor axis b (x-direction), the period P, the thickness of gold film t, the thickness of photoresist film h, the refractive index of medium is n_d, photoresist n_{ph}, and substrate n_{sub}.

The sensing characteristics of the GENAs are analyzed by the Finite Difference Time Domain (FDTD) software (Lumerical Inc., Vancouver, Canada) with full 3-D models. In the model, the simulation domain uses anti-symmetric, symmetric, and perfectly matched layer boundary conditions in the x, y, and z boundaries, respectively. A plane wave source polarizing along the x direction is normally incident on the GENAs. The minimum mesh size is four nanometers. A frequency domain profile monitor has been put above the structure to collects the transmission spectrum through the GENAs. The photoresist is AZ P4620 $(n_{ph} = 1.635)$. The substrate is quartz $(n_{sub} = 1.463)$. Meanwhile, the refractive index of the gold is modeled by fitting to the experimental values in the CRC chemistry and physics handbook (Supplementary part 1). Fig. 5(a) displays the transmission spectra of the GENA structure with water and the different concentrations of NaCl solution (5%, 10%, and 15%). There is one peak obviously red-shifted from 814 nm to 829 nm. In the insert of Fig. 5(a), the fitting curve of the wavelength and refractive index data of NaCl solutions demonstrates good linearity. It is used for calculating the sensitivity of the biosensor, i.e., the value of the variation of the peak wavelength divided by the variation of the refractive index is a constant S ($S = \Delta\lambda/\Delta n$, where $\Delta\lambda$ is the wavelength shift of transmission peaks with the covering medium refractive index variation Δn). Then, the S of the transmission

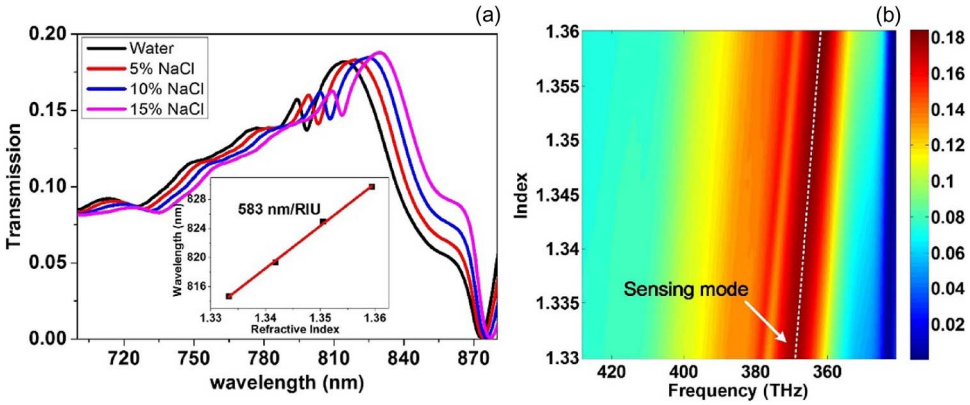

Fig. 5. (a) Simulation of the transmission spectra of a GENA with $P = 600$ nm, $a = 235$ nm, $b = 205$ nm, $h = 180$ nm, and $t = 60$ nm. The insert figure shows the linear fitting between the wavelengths of transmission peak and the covering medium refractive index n_d. (b) FDTD simulation data for the GENA transmission in a large range n_d. High and low transmittance is, respectively, scaled in red and blue. The white dashed line shows the transmission peak position.

peak is 583 nm/RIU. There is also other peak shifts from 794 nm to 809 nm with n_d changing. While this peak intensity is weaker than the previous one, so unsuitable to be as a sensing mode in the experiment. Also, there are some other weak modes in the transmission spectra, leading to some small fluctuations of the transmission spectra (Supplementary part 2). Fig. 5(b) shows the transmission spectra map of the GENAs with n_d tuned from 1.33 to 1.36. In the figure, high and low transmittance is respectively scaled by red and blue color. The white dashed line shows the sensing mode, which shifts with the n_d changing.

The nanocavity structure could be considered as the combination of the nanohole and nanodisk structure. Fig. 6(a)–(c) are the *XZ* cross-section schematic of the nanodisk, nanohole and nanocavity structure, respectively. Fig. 6(d) shows the transmission spectra of the three nanostructures covered by water medium. The blue, red and black lines show the transmission spectrum of the nanodisk, nanohole and nanocavity, respectively. There is no peak in the transmission spectrum of the nanodisk. But one peak exists in the transmission spectrum of the nanohole at 794 nm. Fig. 6(e) is the calculated electric field intensity distribution of the nanohole *XZ* cross-section at this wavelength. There are higher intensity localized electric field in the edge of air hole in gold film. The 794 nm peak also appears in the transmission spectrum of the gold nanocavity, but a stronger peak is excited at 814 nm. Fig. 6(f) and (g) are the calculated steady-state time-averaged total electric field intensity distribution of the nanocavity *XZ* cross-section at 794 nm and 814 nm, respectively. The electric field distributions of the two peaks are similar. However, the electric field of the 814 nm peak is more localized and stronger than the 794 nm peak. The distance between the upper part and the bottom part of the gold is 120 nm, so there is interaction between the two parts [12], [29]. The 814 nm peak of the nanocavity is a peak of a coupled mode. Fig. 6(g) shows that there is stronger and more localized electric field at the edges of the upper part and the bottom part of the gold. Because of the good contact interface between the edge of the upper part of the gold and the medium, a little refractive index change of the medium can lead to large electric field intensity variation at the edge of the upper part of the gold. Then the transmission peak of the coupled mode would has prominent shift vary with the variation of the electric field intensity. Therefore, the coupled mode has high sensitivity.

Based on the simulation results, the suitable GENAs sample was fabricated by the TPNL with an incident laser power of 1.202 mW. Each elliptic nanohole was exposed 40 ms. Fig. 7(a) shows the scanning electron microscope (SEM) image of one GENA with $P = 600$ nm, $t = 60$ nm, $h = 180$ nm, $a = 235$ nm, and $b = 205$ nm. The transmission spectra of the chip are measured in four different concentrations of NaCl solutions. All the spectra are normalized in Fig. 7(b). The insert figure shows the enlargement of the peaks of the coupled mode. The wavelengths of peaks are clearly red shifted as n_d increases. In Fig. 7(c), the shift of the peaks is

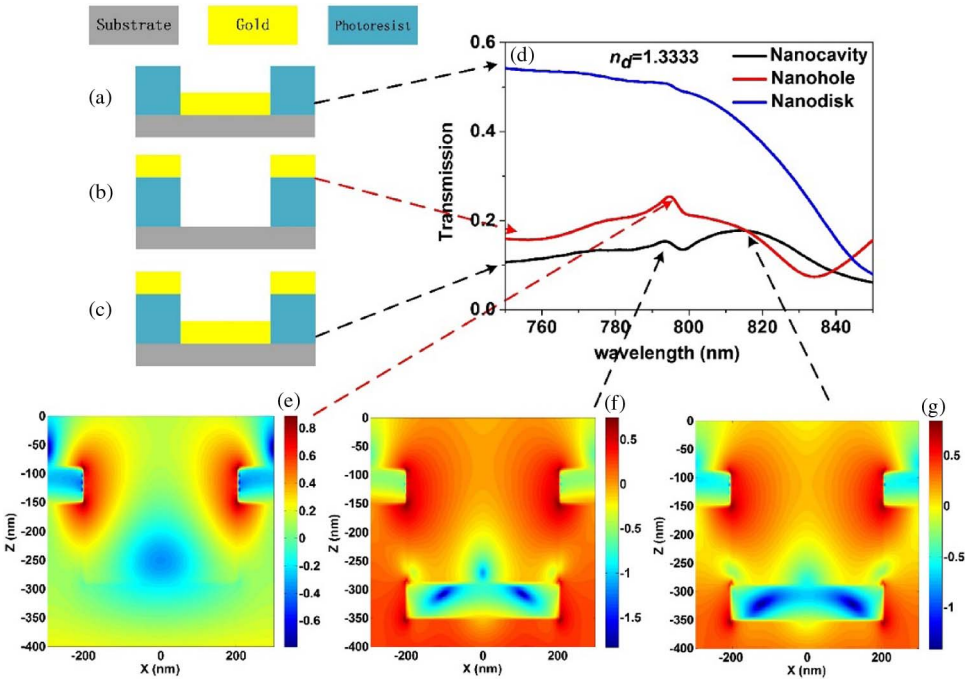

Fig. 6. Simulation of the optical properties of the nanodisk, nanohole, and nanocavity arrays. The nanocavity is the same as in Fig. 5(a). The nanodisk and nanohole are the same as the nanocavity, except there is no upper part or bottom part of the gold, respectively. (a)–(c) The *XZ* cross-section schematic of the nanodisk, nanohole and nanocavity structure, respectively. (d) The transmission spectra of the nanodisk, nanohole, and nanocavity structure with the medium of water. (e)–(g) Log 10-scale plots of the electric field intensity with the medium of water of *XZ* cross-section of the nanohole and nanocavity at the wavelengths of the transmission peaks. Note the different color bar; the electric field intensities are different in the three figures.

linear with the n_d. The *S* of this chip is 562 nm/RIU. It's higher than that of other previously reported nanoperiod arrays with similar period and measurement wavelength regime [17], [30]. Comparing *S* of the experiment to the simulation, experiment determined *S* is about 30 nm/RIU less than that of the simulation. Fig. 7(d) displays the simulation and experiment transmission spectra of the GENAs with the covering medium of water. The black and blue lines are the simulation transmission spectrum of the GENA in Fig. 6(c) and the measurement transmission spectrum of the GENA in Fig. 7(a), respectively. Compared with the simulation results, the measurement transmission spectrum has some differences. The peak of the measurement transmission spectrum has been blue shifted and broadened, and the transmission peaks of the other modes disappear in the measurement spectrum. In fact, this differences exist in all chips we fabricated. While in the gold EBE process, a small amount of the gold will deposit on the sidewall of the photoresist which is partly responsible for the differences. Then the actual cross-section is not the same as that Fig. 6(c) shows, thus the gold on the sidewall can connect the upper part and the bottom part of the gold. So the coupled mode would be affected by the gold sidewall. The inset figure of Fig. 7(d) shows the *XZ* cross-section schematic diagram of the GENA with 4 nm gold sidewall which connects the upper part and the bottom part of the gold. The red line in Fig. 7(d) is the simulation transmission spectrum of the connected GENAs. Compared to the simulation transmission spectrum of the disconnected one, the peaks of the connected GENAs are blue shift, and the peak at short wavelength is weaken (Supplementary part 3). These phenomena are attributed to the change of the interaction between the nanohole and nanodisk, which would be resulted from the gold on the sidewall. The simulated S of the connected GENAs is 574 nm/RIU, which is lower than the disconnected one (Supplementary part 4). Therefore, the gold sidewall is one reason for the low *S*, blue shift, and disappearing of the short

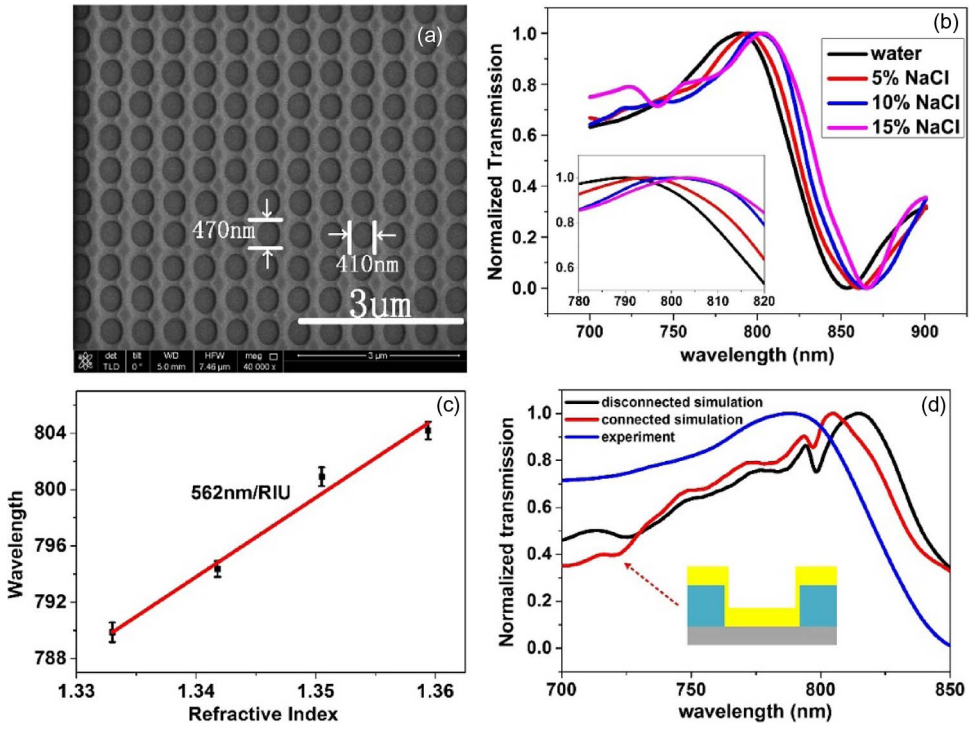

Fig. 7. (a) SEM image of the GENA structure ($P = 600$ nm, $a = 235$ nm, $b = 205$ nm, $h = 180$ nm, and $t = 60$ nm). (b) The measurement transmission spectra of the GENA in (a) in the four testing samples. The transmission peak of the coupled mode is red shift with n_d increasing. Inset in (b) shows the detail of the peak shift. (c) Linear fitting between the wavelengths of the transmission peaks and n_d. The S of the nanostructure is 562 nm/RIU. (d) The transmission spectra of measurement and simulation with the medium of water. All of the transmission spectra are normalized. Inset in (d) shows the XZ cross-section schematic of the connected nanocavity. The thick of the connected gold film is 4 nm.

wavelength peaks in experiment transmission spectra. As shown in Fig. 7(d), there are also some differences between the measurement transmission spectrum and the simulation transmission spectrum of the connected GENAs, which may be caused by the rough surface of the gold film and non-uniformity of the elliptic nanocavity induced from the fabrication process, such as Au EBE and TPNL [11]. The surface roughness of the gold film can cause stronger plasmon coupling to the scattering losses leading to shorter plasmon propagation lengths and spectrally broader resonances [18]. The transmission spectra depend on the structural parameters of the GENAs. The different transmission spectra of different size GENA units are overlapped to be the measurement transmission spectra so that the transmission spectra become broader and the peaks of the weak modes are disappearing [26].

There are two potential ways to improve the sensitivity of the GENAs biosensor chip. One is to design new nanostructures and to optimize the structural parameters [6]. The other one is to optimize the fabrication process to smooth the gold film surface and accurately achieve the uniform nanocavity arrays [18].

4. Conclusion

GENAs biosensor chip, which works under the coupled mode transmission, is designed, simulated, fabricated, and characterized. The GENA with dimension of $P = 600$ nm, $t = 60$ nm, $h = 180$ nm, $a = 235$ nm, and $b = 205$ nm is fabricated by the suitable TPNL. Then the GENA and PDMS with microchannels are bonded together to form a sensor chip. The sensitivity of the GENA biosensor chip is characterized by the water and the different concentrations of NaCl

solution. The peak of the coupled mode transmission of biosensor chip shows higher sensitivity which reaches 562 nm/RIU. The GENA, which is easily and cost-effectively fabricated by TPNL, is a potential biosensor chip widely used in label-free chemical and biomedical fields, especially cancer biomarker testing.

References

[1] T. W. Ebbesen *et al.*, "Extraordinary optical transmission through sub-wavelength hole arrays," *Nature*, vol. 391, no. 6668, pp. 667–669, Feb. 1998.
[2] Z. C. Ruan and M. Qiu, "Enhanced transmission through periodic arrays of subwavelength holes: The role of localized waveguide resonances," *Phys. Rev. Lett.*, vol. 96, no. 23, Jun. 2006, Art. ID. 233901.
[3] H. T. Liu and P. Lalanne, "Microscopic theory of the extraordinary optical transmission," *Nature*, vol. 425, no. 7188, pp. 728–731, Apr. 2008.
[4] J. M. Pitarke, V. M. Silkin, E. V. Chulkov, and P. M. Echenique, "Theory of surface plasmons and surface-plasmon polaritons," *Rep. Progr. Phys.*, vol. 70, no. 1, pp. 1–87, Jan. 2007.
[5] F. J. Garcia-Vidal, L. Martin-Moreno, T. W. Ebbesen, and L. Kuipers, "Light passing through subwavelength apertures," *Rev. Mod. Phys.*, vol. 82, no. 1, pp. 729–787, Mar. 2010.
[6] M. Couture *et al.*, "Tuning the 3D plasmon field of nanohole arrays," *Nanoscale*, vol. 5, no. 24, pp. 12 399–12 408, Dec. 2013.
[7] A. E. Cetin *et al.*, "Handheld high-throughput plasmonic biosensor using computational on-chip imaging," *Light, Sci. Appl.*, vol. 3, no.1, p. e122, Jan. 2014.
[8] T. Hanke *et al.*, "Tailoring spatiotemporal light confinement in single plasmonic nanoantennas," *Nano Lett.*, vol. 12, no. 2, pp. 992–996, Feb. 2012.
[9] M. X. Ren, E. Plum, J. J. Xu, and N. I. Zheludev, "Nanostructured plasmonic medium for terahertz bandwidth all-optical switching," *Adv. Mater.*, vol. 23, no. 46, pp. 5540–5544, Dec. 2011.
[10] J. M. Liu, J. T. Chen, and X. P. Yan, "Near infrared fluorescent trypsin stabilized gold nanoclusters as surface plasmon enhanced energy transfer biosensor and in vivo cancer imaging bioprobe," *Anal. Chem.*, vol. 85, no. 6, pp. 3238–3245, Mar. 2013.
[11] K. L. Lee, J. T. Tsai, M. J. Chih, Y. D. Yao, and P. K. Wei, "High-throughput label-free detection using a gold nanoslit array with 2-D spectral images and spectral integration methods," *IEEE J. Sel. Topics Quantum Electron.*, vol. 19, no. 3, May/Jun. 2013, Art. ID. 4800407.
[12] Y. Shen *et al.*, "Plasmonic gold mushroom arrays with refractive index sensing figures of merit approaching the theoretical limit," *Nat. Commun.*, vol. 4, no. 2381, pp. 1–9, Aug. 2013.
[13] M. R. Jones, K. D. Osberg, R. J. Macfarlane, M. R. Langille, and C. A. Mirkin, "Templated techniques for the synthesis and assembly of plasmonic nanostructures," *Chem. Rev.*, vol. 111, no. 6, pp. 3736–3827, Jun. 2011.
[14] Z. Y. Fang and X. Zhu, "Plasmonics in nanostructures," *Adv. Mater.*, vol. 25, no. 28, pp. 3840–3856, Jul. 2013.
[15] B. Sciacca and T. M. Monro, "Dip biosensor based on localized surface plasmon resonance at the tip of an optical fiber," *Langmuir*, vol. 30, no. 3, pp. 946–954, Jan. 2014.
[16] L. H. Zhao *et al.*, "Enhanced light extraction of InGaN LEDs with photonic crystals grown on p-GaN using selective-area epitaxy and nanospherical-lens photolithography," *J. Semicond.*, vol. 34, no. 10, Oct. 2013, Art. ID. 104005.
[17] Y. D. Chuo *et al.*, "Large-area low-cost flexible plastic nanohole arrays for integrated bio-chemical sensing," *IEEE Sensors J.*, vol. 13, no. 10, pp. 3982–3900, Oct. 2013.
[18] A. A. Yanik *et al.*, "Seeing protein monolayers with naked eye through plasmonic Fano resonances," *Proc. Nat. Acad. Sci. USA*, vol. 19, no. 108, pp. 11 784–11 789, Jul. 2011.
[19] X. J. Ni, S. Ishii, A. V. Kildishev, and V. M. Shalaev, "Ultra-thin, planar, Babinet-inverted plasmonic metalenses," *Light, Sci. Appl.*, vol. 2, no.4, p. e72, Apr. 2013.
[20] Z. B. Sun *et al.*, "Multicolor polymer nanocomposites: In situ synthesis and fabrication of 3D microstructures," *Adv. Mater.*, vol. 20, no. 5, pp. 914–919, Mar. 2008.
[21] S. Kawata, H. B. Sun, T. Tanaka, and K. Takada, "Finer features for functional microdevices," *Nature*, vol. 412, no. 6848, pp. 697–698, Aug. 2001.
[22] J. F. Xing *et al.*, "Improving spatial resolution of two-photon microfabrication by using photoinitiator with high initiating efficiency," *Appl. Phys. Lett.*, vol. 90, no. 13, Mar. 2007, Art. ID. 131106.
[23] H. Z. Cao *et al.*, "Direct writing of shape-controlled nanodot array by two-photon nanolithography using elliptic beam," *Appl. Phys. Exp.*, vol. 6, no. 6, May 2013, Art. ID. 066501.
[24] H. Z. Cao *et al.*, "Two-photon nanolithography of positive photoresist thin film with ultrafast laser direct writing," *Appl. Phys. Lett.*, vol. 102, no. 20, May 2013, Art. ID. 201108.
[25] J. A. Ruemmele, W. P. Hall, L. K. Ruvuna, and R. P. Van Duyne, "A localized surface plasmon resonance imaging instrument for multiplexed biosensing," *Anal. Chem.*, vol. 85, no. 9, pp. 4560–4566, May 2013.
[26] Z. X. Geng, Q. Kan, J. Yuan, and H. D. Chen, "A route to low-cost nanoplasmonic biosensor integrated with optofluidic-portable platform," *Sens. Actuators B, Chem.*, vol. 195, pp. 682–691, May 2014.
[27] C. Escobedo, "On-chip nanohole array based sensing: A review," *Lab Chip*, vol. 13, no. 13, pp. 2445–2463, Jul. 2013.
[28] S. Roh, T. Chung, and B. Lee, "Overview of the characteristics of micro- and nano-structured surface plasmon resonance sensors," *Sensors*, vol. 11, no. 2, pp. 1565–1588, 2011.
[29] Y. Gu, Q. Z. Li, and G. P. Wang, "Dielectric supported ring-shaped metal disks on a metal film for ultrasensitive refractive index sensing," *Opt. Lett.*, vol. 36, no. 17, pp. 3326–3328, Sep. 2011.
[30] J. S. Kee, S. Lim, A. P. Perera, M. K. Park, and Y. Zhang, "Plasmonic nanohole array for biosensor applications," *Proc. IEEE PGC*, 2012, pp. 1–4.